Nonthermoelastic martensitic features in ideal martensites due to volume effects

Yuanchao Yang,[1] Yangyang Xu,[1] Yumei Zhou,[1,*] Xiangdong Ding,[1] Jun Sun,[1] Turab Lookman,[2,†] and Dezhen Xue[1,‡]
[1]*State Key Laboratory for Mechanical Behavior of Materials, Xi'an Jiaotong University, Xi'an 710049, China*
[2]*AiMaterials Research, Santa Fe, New Mexico 87501, USA*

(Received 18 April 2023; revised 27 June 2023; accepted 29 June 2023; published 18 July 2023)

We study martensitic transformation behavior by considering the coupling of volumetric strain and the transformation strain in a group-subgroup transformation within a Ginzburg-Landau framework. Nonthermoelastic features, including large residual strain, large thermal hysteresis, and incomplete transformation gradually, appear with increasing coupling strength. The volume change associated with the transformation due to the coupling is demonstrated to be the essential physics for nonthermoelastic features that appear in an ideal thermoelastic martensitic transformation. A materials descriptor for features associated with a martensitic transformation is proposed based on insights from the model.

DOI: 10.1103/PhysRevB.108.024102

I. INTRODUCTION

The martensitic transformation (MT) is a solid-to-solid phase transformation in alloys, ceramics, and proteins characterized by a diffusionless, shear driven movement of atoms [1–4]. The resultant rich microstructures and functionalities have led to various technological applications such as enhancement of the strength of steel, improvement of toughness in yttria-stabilized zirconia ceramics, and the shape memory and superelastic effects in shape memory alloys (SMAs) [1,5,6]. Thus, the means to control mechanisms that influence the evolution and microstructure of MTs is scientifically and technologically important.

In SMAs, the MT is thermoelastic and completely reversible [7,8]. Upon cooling from high temperature, the high symmetry parent phase transforms into the low symmetry martensite phase with twinned microstructure that disappears on reheating to the parent phase. The process is reversible. Moreover, martensite can also be induced by applying stress and the phase can be reversed to the parent on unloading. The elastic compatibility between parent phase and martensite leads to a coherent interface, which is very mobile during the temperature or stress induced MT without the appearance of irreversible dislocations [9,10]. As a result, such an ideal thermoelastic MT possesses features such as small thermal hysteresis, little residual martensite, and good cyclic stability [11–13].

In contrast, the MT in alloys such as steels, CoNi, and FeNi, is nonthermoelastic with characteristics of irreversibility [2,8]. A microstructure with a lenticular morphology appears in sudden bursts upon cooling from the parent phase; however, it does not disappear upon reheating [7,14] so that the process is irreversible. Moreover, the nonthermoelastic MT is always incomplete, with residual parent phase at low temperature and residual martensite at high temperature [15–17]. Thus the motion of the interface between two phases is hindered upon temperature change or external stress and irreversible dislocations are inevitably generated and accumulated [8]. As a result, such a nonthermoelastic MT has large thermal hysteresis, residual phases, and poor cyclic stability.

The intrinsic origin of the above differences between thermoelastic and nonthermoelastic MTs lies in the symmetry change during the transformation. It has been pointed out that that the symmetry groups of the parent and martensite phases need to have a group-subgroup relationship as a necessary condition for reversibility. Interestingly, it has been observed experimentally that nonthermoelastic features appear in thermoelastic martensitic transformation systems [18,19]. Moreover, the nonthermoelastic feature of lenticular structure appears as a result of volume change. [20]. However, the differences between the thermoelastic and the nonthermoelastic features have not been modeled [7,21–24]. In the present study, we propose a Ginzburg-Landau model to uncover the mechanisms of thermoelastic martensitic systems with nonthermoelastic features.

In the model, we couple the volumetric strain (e_1) with the order parameter deviatoric shear strain (e_2). With increasing coupling strength, features of nonthermoelastic MT including large residual strain, large thermal hysteresis, and incomplete transformation appear. Such an evolution is attributed to the appearance of volumetric strain (e_1) during the transformation as a result of the coupling between e_1 and e_2. This coupling hinders the growth of martensite by penalizing further transformation. As the basic physics we include in the model demands continuity of displacements, the elastic fields are forced to satisfy compatibility as we do not include a source for dislocations. Nevertheless, we tested the validity of both the linear and nonlinear strain compatibility equations as a function of the coupling strength. We performed two-dimensional (2D) time-dependent simulations and showed that the thermal hysteresis increases with the coupling strength as a result of heating and cooling. The morphology after the transformation consists of lenticular

*zhouyumei@xjtu.edu.cn
‡xuedezhen@xjtu.edu.cn
†turablookman@gmail.com

martensite within the untransformed austenite matrix. On heating, residual martensite persists at higher temperatures and its fraction increases with the coupling strength. As the coupling strength increases, we monitor the deviation in the elastic compatibility relation as the system tries to accommodate the effects of the volume. We propose a materials descriptor for the volume change in terms of the strains and show how it captures the tendency of the thermal hysteresis behavior in a number of shape memory alloys.

The paper is organized as follows. In Sec. II, we discuss the mesoscale model that captures the salient aspects of martensitic transformation. Section III gives the model results showing that the transformation behavior and microstructure vary with coupling strength. Section IV discusses the reasons for the emergence of nonthermoelastic features and predicts phenomena that can be experimentally validated. We summarize the main results in Sec. V and provide further applications of the model.

II. FORMULATION OF THE GINZBURG-LANDAU MODEL

A. Free energy

We consider a two-dimensional model system with a first-order square-to-rectangle martensitic transformation [25–29]. As shown in Fig. 1, the martensitic transformation is driven by a deviatoric strain order parameter (OP) $e_2 = \frac{1}{\sqrt{2}}(\varepsilon_{xx} - \varepsilon_{yy})$ which describes the tetragonal distortions, where $\varepsilon_{ij} = \frac{1}{2}(\frac{\partial u_i}{\partial x_j} + \frac{\partial u_j}{\partial x_i})$ is the linearized strain tensor. There exist other symmetry adapted combinations of the strain tensor components, including the volumetric strain $e_1 = \frac{1}{\sqrt{2}}(\varepsilon_{xx} + \varepsilon_{yy})$ and the simple shear stain $e_3 = \varepsilon_{xy}$. The total free energy density is thus given by

$$f = f_{\text{OP}} + f_{\text{gradient}} + f_{\text{non-OP}} + f_{\text{coupling}}, \tag{1}$$

where f_{OP} is the homogeneous Landau contribution representing the free energy for a square-to-rectangle distortion, f_{gradient} is the gradient term responsible for the interface energy, and $f_{\text{non-OP}}$ represents the non-OP part of the elastic free energy due to e_1 and e_3. The f_{OP} is given by

$$f_{\text{OP}} = \tfrac{1}{2}A_2(T){e_2}^2 + \tfrac{1}{4}\beta {e_2}^4 + \tfrac{1}{6}\gamma {e_2}^6, \tag{2}$$

where $A_2 = (C_{11} - C_{12})$ and depends on temperature via $A_2(T) = A_2T_0(\tau - 1)$. The $\tau = \frac{T}{T_0}$ is the scaled temperature and T_0 is the transition temperature. The f_{gradient} is given by

$$f_{\text{gradient}} = \tfrac{1}{2}g|\nabla e_2|^2, \tag{3}$$

where g is the interfacial energy. $f_{\text{non-OP}}$ is assumed to be harmonic and is given by

$$f_{\text{non-OP}} = \tfrac{1}{2}A_1{e_1}^2 + \tfrac{1}{2}A_3{e_3}^2, \tag{4}$$

where $A_1 = C_{11} + C_{12}$ and $A_3 = 4C_{44}$ are the elastic moduli calculated from C_{11}, C_{12}, and C_{44}, the elastic constant tensor components. f_{coupling} describes the coupling between e_2 and e_1, and will be discussed in the next subsection.

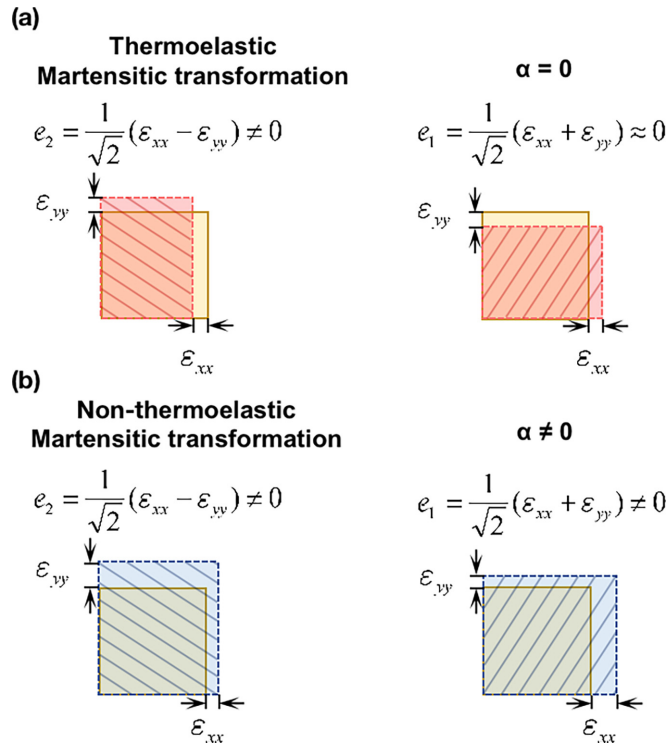

FIG. 1. The schematics for the thermoelastic and nonthermoelastic martensitic features. The yellow squares with solid frame represent the austenite. The red rectangles and blue rectangles with dashed frame are the variants of martensite for thermoelastic martensitic transformation and nonthermoelastic features. The order parameter deviatoric strain e_2 is nonzero once the transformation occurs. The volumetric strain e_1 is close to zero in martensite for thermoelastic transformation (a), in contrast to the nonthermoelastic features (b) where e_1 is finite.

B. Coupling between volumetric strain and deviatoric shear strain

As shown in Fig. 1(a), during the thermoelastic martensitic transformation, the deviatoric strain $e_2 \neq 0$, whereas the volumetric strain $e_1 \approx 0$. For nonthermoelastic martensitic transformation, both $e_2 \neq 0$ and the volumetric strain e_1 depart from 0, as shown in Fig. 1(b).

To realize the two types of martensitic transformations in a unified model, we introduce a term in the free energy that couples the deviatoric and volumetric strains, i.e.,

$$f_{\text{coupling}} = \alpha e_1{e_2}^2, \tag{5}$$

where α controls the coupling strength between e_1 and e_2. As e_2 becomes nonzero during the course of the phase transformation, the coupling accentuates the volume strain e_1, which starts to hinder the transformation with non thermoelastic features. Without the coupling, e_1 is not appreciably influenced by e_2 and thus we obtain the usual thermoelastic martensitic features. The total free energy is given by

$$F = \int d\vec{r}(f_{\text{OP}} + f_{\text{gradient}} + f_{\text{non-OP}} + f_{\text{coupling}}). \tag{6}$$

C. Dynamic evolution

The dynamic equations for the free energy is written in terms of the displacement fields by means of force balance equations given by

$$\rho \ddot{\vec{u}} = \nabla \cdot \vec{\sigma}. \tag{7}$$

Here the elastic stresses are obtained from the total free energy in Eq. (6) as

$$\sigma_{ij} = \sum_k \frac{\delta F}{\delta e_k} \frac{\delta e_k}{\delta \varepsilon_{ij}}. \tag{8}$$

The equations of motion for the displacement variables u_i become

$$\begin{aligned} \frac{\partial^2 u_x}{\partial t^2} &= \frac{\partial \sigma_{xx}}{\partial x} + \frac{\partial \sigma_{xy}}{\partial y}, \\ \frac{\partial^2 u_y}{\partial t^2} &= \frac{\partial \sigma_{xy}}{\partial x} + \frac{\partial \sigma_{yy}}{\partial y}. \end{aligned} \tag{9}$$

The total stress fields are determined from the elastic free energy using

$$\begin{aligned} \sigma_{xx} &= \frac{G_1}{\sqrt{2}} + \frac{G_2}{\sqrt{2}}, \\ \sigma_{yy} &= \frac{G_1}{\sqrt{2}} - \frac{G_2}{\sqrt{2}}, \\ \sigma_{xy} &= G_3, \end{aligned} \tag{10}$$

where

$$\begin{aligned} G_1 &= \frac{\partial F}{\partial e_1} = A_1 e_1 + \alpha e_2^2, \\ G_2 &= \frac{\partial F}{\partial e_2} = A_2 e_2 + \beta e_2^3 + \gamma e_2^5 + g(\nabla^2 e_2) + 2\alpha e_1 e_2, \\ G_3 &= \frac{\partial F}{\partial e_3} = A_3 e_3. \end{aligned} \tag{11}$$

Finally, the transformation behavior and microstructure associated with the square-to-rectangle transformation as a function of temperature for different values of coupling coefficient α are simulated using the equations of motion.

The continuum model is implemented numerically on a two-dimensional 256×256 lattice with periodic boundaries. An Euler level scheme is found to be adequate for capturing the salient features with discretization $\delta x = 1$, $\delta y = 1$, and $\delta t = 0.02$. However, we also used a fourth-order Runge-Kutta (RK4) scheme to study the influence on the linear and nonlinear strain compatibility relationships as α increases. We choose reduced values for the parameters appropriate for FePd [30]: $A_1 = 1.0$, $A_2 = 2.27$, $A_3 = 4.54$, $\beta = -276$, $\gamma = 4.86 \times 10^5$. The thermal cycling simulations start from austenite with $e_2 = 0$ at $\tau = 2.0$. A random fluctuation was introduced to every site so that the variants are randomly nucleated during cooling. A stepwise cooling procedure was employed and the system evolves for 1000 steps at each temperature interval of 0.01.

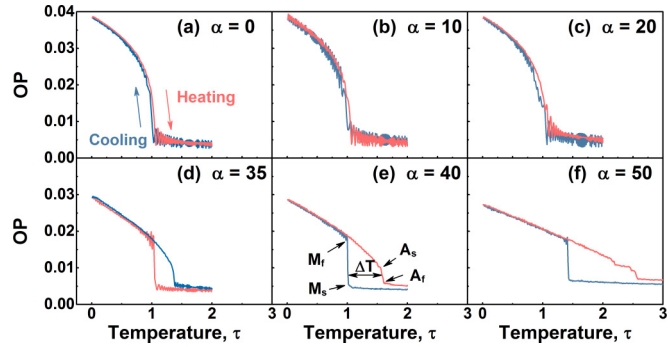

FIG. 2. The order parameter (OP) as a function of temperature for different values of α. (a) $\alpha = 0$, (b) $\alpha = 10$, (c) $\alpha = 20$, (d) $\alpha = 35$, (e) $\alpha = 40$, and (f) $\alpha = 50$. The data shown are for the second thermal cycle. The start and finish temperatures of martensitic transformation are M_s and M_f; the start and finish temperatures of reverse transformation are A_s and A_f. The temperatures were obtained by the tangent method.

III. RESULTS

We present the effects of the coupling on the martensitic transformation related to (1) the transformation behavior, (2) the microstructure evolution, and (3) the thermal cycling behavior.

A. The effects of coupling e_1 and e_2 on the transformation behavior

It has been shown experimentally that the transformation temperatures, especially the reverse transformation temperature, are fairly high in nonthermoelastic MT alloys such as Fe-C steels and FeNi alloys [16,31]. Moreover, a thermal hysteresis larger than 100 K is always observed in Fe-Mn-Si-Cr-Ni [32], FeMnSi [33], and FeNiCoAl [34] systems with nonthermoelastic MT. There also exists a clear residual strain after thermal cycling in nonthermoelastic systems such as CoNi and FeMnCrSiNi [16,35]. We first investigate the influence of coupling on the transformation temperature, thermal hysteresis, and residual strain.

Figure 2 shows the order parameter e_2 as a function of temperature for different coupling strengths $\alpha = 0$, 10, 20, 35, 40, and 50. The order parameter is calculated by averaging the absolute value of e_2 over the entire system. The two curves in each panel correspond to cooling (blue) and heating (red) processes for the second thermal cycle where the strains evolve to finite values. As the transformation is first order, the deviatoric strain e_2 deviates at the transformation temperature regardless of the value of α. However, the transformation temperature increases with α. For $\alpha = 0$–20, the thermal hysteresis is small with the heating and cooling curves essentially overlapping. For α from 35 to 50, the thermal hysteresis is large.

As shown in Fig. 2(e), the start and finish temperatures of the martensitic transformation (M_s and M_f) and the start and finish temperatures of the reverse transformation (A_s and A_f) were obtained by the tangent method from the order parameter versus temperature curve. The exponential increase in A_f and M_s as a function of α is shown in Fig. 3(a) with A_f increasing more dramatically than M_s. Figure 3(b) shows the exponential

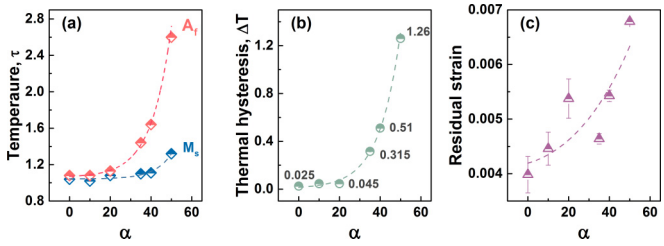

FIG. 3. The features are plotted as a function of coupling strength α. The dotted lines are the fits to the data based on exponential growth. (a) The transformation temperatures as a function of α following $M_s = 1.04 + 0.01e^{0.1\alpha}$ and $A_f = 1.06 + 0.01e^{0.1\alpha}$. (b) The thermal hysteresis $\Delta T = \frac{(A_s+A_f)-(M_s+M_f)}{2}$ as a function of α following $\Delta T = 0.0047 + 0.1e^{0.1\alpha}$. (c) The residual strain (RS) as a function of α following $\mathrm{RS} = 0.06 + 0.06e^{0.0007\alpha}$.

increase in thermal hysteresis ΔT versus α. ΔT is calculated from $\Delta T = \frac{(A_s+A_f)-(M_s+M_f)}{2}$. For α small, the values of A_f, M_s, and ΔT, are quite stable but increase sharply for $\alpha = 35$, which is a critical point indicating that the nonthermoelastic features emerge.

The coupling strength α also affects the residual strain, the difference in the order parameter e_2 of the austenite under cooling and heating (Fig. 2). The values of austenite were determined from the average value of e_2 within the temperature range 1.60–1.9 for α smaller than 40 and within the range 2.6–2.9 for $\alpha = 50$. The error bar represents the 95% confidence interval in the order parameter in the above temperature range. Figure 3(c) shows that the residual strain increases with α, the dotted line indicates a fit to the data based on exponential growth. The residual strain here is defined as the difference between the order parameter (OP) strains at a given temperature after cooling and heating during one thermal cycle. Thus, Figs. 2 and 3 reveal that aspects of nonthermoelastic features appear as the result of the coupling. And the transformation features (P) including transformation temperature, thermal hysteresis, and residual strain all increase with α following a functional form of the exponential behavior, $P = A + Be^{\alpha}$.

B. The effects of coupling e_1 and e_2 on the microstructure

Figure 4 shows the variation of typical configurations and the corresponding distribution of e_2 as a function of heating and cooling for different coupling strength α.

For $\alpha = 0$, 10, and 20, thermoelastic martensite with a typical polytwinned microstructure is formed on cooling and then transforms back to austenite on heating at almost the

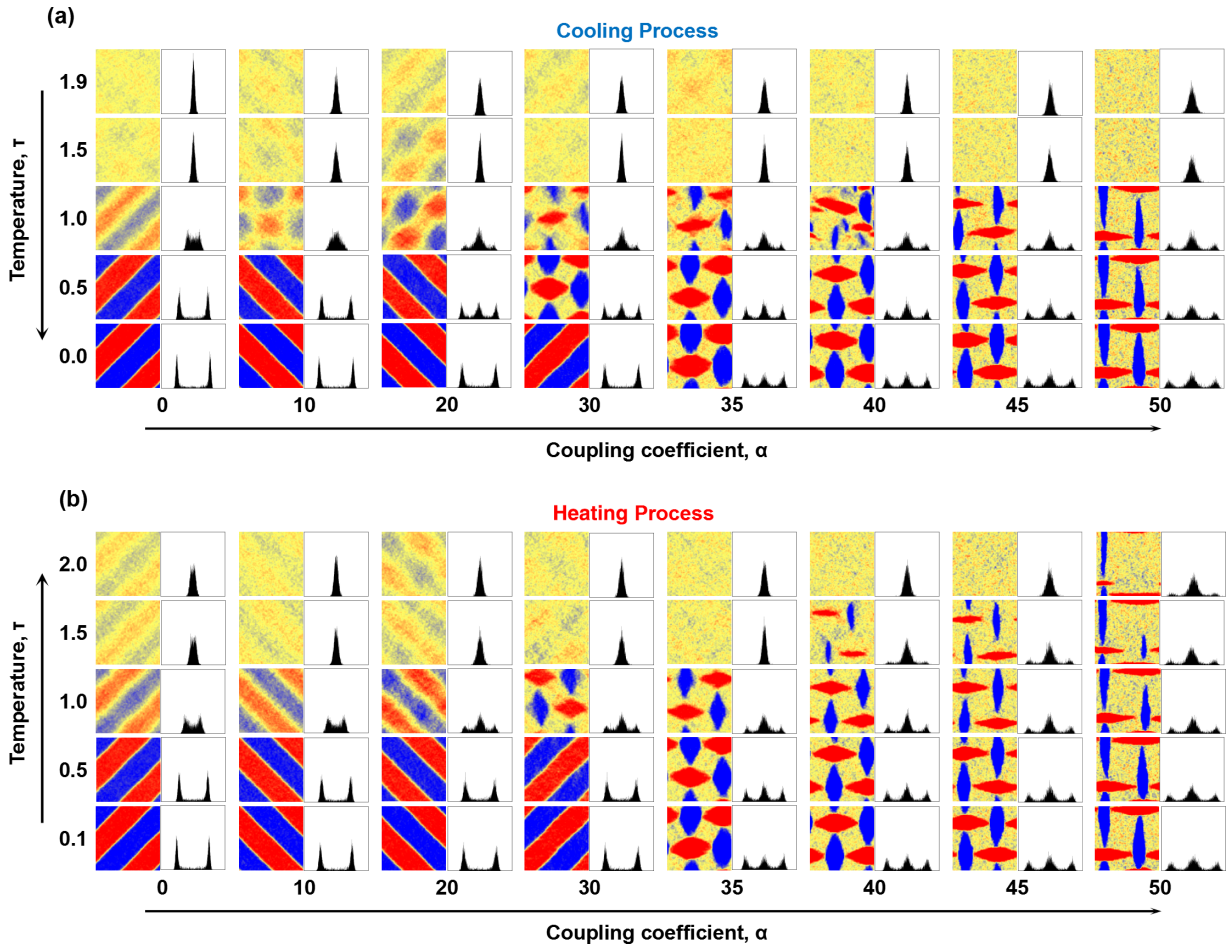

FIG. 4. Snapshots of selected configurations for eight different values of α as a function of temperature for (a) cooling process and (b) heating process. Yellow color represents the parent phase; blue and red colors represent the two martensite variants. The local strain distribution is shown by the probability density function (pdf) with respect to the order parameter e_2.

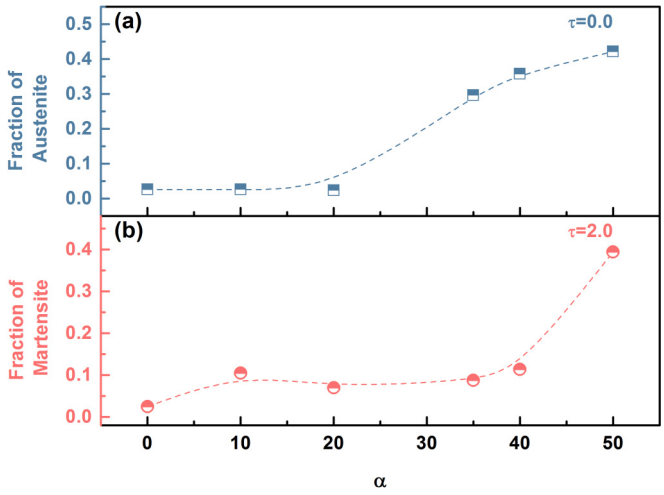

FIG. 5. The fraction of residual martensite and austenite as a function of α. (a) The fraction of austenite at $\tau = 0.0$. (b) The fraction of martensite at $\tau = 2.0$.

same temperature. The corresponding local strain distribution also transforms from a single peak around zero austenite to a distribution with two sharp peaks corresponding to the two degenerate states of martensite. When α increases to 35, 40, and 45, the system transforms into a system with lenticular martensite, which is similar to nonthermoelastic martensite structure. It is seen that the austenite in yellow is retained and coexists with martensite at low temperatures ($\tau \leqslant 1.0$). This is consistent with the corresponding local strain distribution with an extra peak around zero in addition to the two peaks for martensite. When heated, it completely transforms back to austenite ($\tau > 1.5$) and the local strain distribution returns to the single peak profile. We note that the size of the lenticular martensite decreases with α. The cooling process for $\alpha = 50$ is similar to that for $\alpha = 45$. However, during the heating process, the martensite cannot transform back to austenite completely, leaving residual martensite up to the temperature limit of our study ($\tau = 2.0$). The three-peak profile of the corresponding local strain also signals the existence of residual martensite. We note that there exists a two-step-like phase transformation with structure which is similar to nonthermoelastic martensite disappearing in the system for $\alpha = 30$. On cooling, austenite transforms first to lenticular martensite with residual austenite (like nonthermoelastic) and then transforms abruptly into martensite with a typical poly-twinned microstructure (thermoelastic).

The existence of residual austenite at low temperature and residual martensite at high temperature in Fig. 4 captures the main features of the experimental observations in most nonthermoelastic alloys such as FeNi [15] and CoNi [36]. Figures 5(a) and 5(b) show the fraction of austenite at $\tau = 0.0$ and that of martensite at $\tau = 2.0$, respectively, during a thermal cycle. With α increasing, the fraction of austenite gradually grows from 0, indicating that the transformation of austenite is arrested by the coupling $\alpha e_1 e_2^2$. The fraction of martensite shows a tendency similar to that of the residual austenite. Thus, the irreversible nonthermoelastic feature appears in the reversible thermoelastic martensitic transformation with raising the coupling strength α.

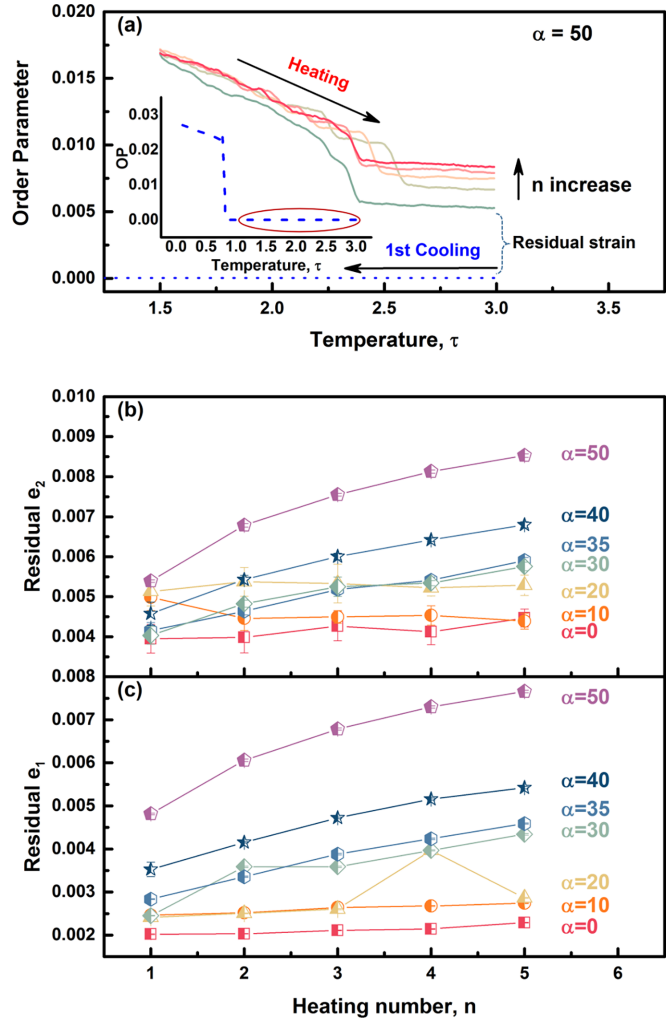

FIG. 6. (a) The transformation dependence on the temperature for $\alpha = 50$ for 5 heating progress. (b)–(c) The relationship between residual strain (e_1 and e_2) and heating number n respectively.

C. The effect of coupling of e_1 and e_2 on thermal cyclic behavior

To further confirm that the large coupling coefficient α leads to nonthermoelastic features, we simulated the characteristic thermal cycling behavior. It has been shown experimentally that more residual strain will be accumulated during thermal cycling for a system with greater degree of nonthermoelastic transformation features [37–39]. We thus carried out five successive thermal cycles for systems with different α. For $\alpha = 50$ as an example, Fig. 6(a) shows the order parameter e_2 as a function of temperature for five successive heating processes. The first cooling process starting from an initial state of $e_2 = 0$ at $\tau = 2.0$ serves as a baseline to calculate the residual strain. The residual e_1 and e_2 are defined as the deviation from the average value of e_1 and e_2 within a small temperature range τ (1.6–1.9) from the baseline (for the system with $\alpha = 50$, τ is within 2.6–2.9). Figures 6(b) and 6(c) show the residual e_1 and e_2 as a function of the cycle number n for different values of α, respectively. The error bar is set as the 95% confidence interval.

For $\alpha = 0$, 10, and 20, the residual strains (e_1 and e_2) change little with increasing cycling number. With increasing

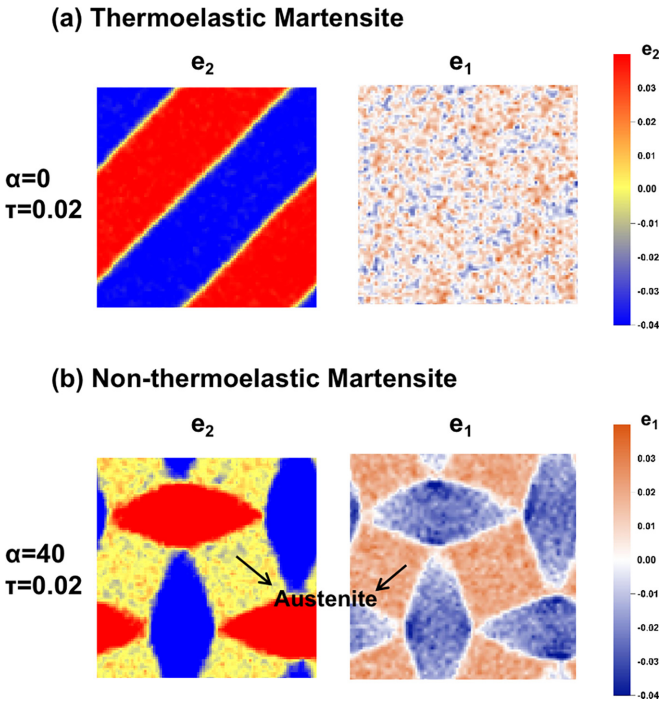

FIG. 7. Spatial distribution of order parameter strain e_2 (left panel) and nonorder parameter strain e_1 (right panel) in (a) a system of thermoelastic martensitic transformation with $\alpha = 0$ and (b) a system of nonthermoelastic martensitic transformation with $\alpha = 40$.

α to 35, 40, and 50, the residual strain (e_1 and e_2) increases with the cycle number. The above results indicate that small α captures the thermal cycle feature of the thermoelastic martensite such as NiTi, whereas the large α limit leads to accumulation of residual strains in nonthermoelastics, such as Fe-based alloys [1].

In summary, coupling between deviatoric strain e_2 and volumetric strain e_1 leads to an increase in the phase transformation temperature, the thermal hysteresis, and the residual strain. In addition, lenticular martensite appears with increasing α, giving rise to an incomplete phase transformation with typical characteristics of a nonthermoelastic martensitic transformation [7,14]. More strain is accumulated continuously with thermal cycling for larger α.

IV. DISCUSSION

We address the underlying physics for ideal thermoelastic martensite with nonthermoelastic features and the experimental validity of the model.

A. Stress concentration at the austenite and martensite phase boundary

We first compare the low temperature microstructures of a typical thermoelastic MT ($\alpha = 0$) and one with nonthermoelastic features (lenticular martensite) ($\alpha = 40$). Figures 7(a) and 7(b) show the morphologies of e_2 (left panel) and e_1 (right panel) at $\tau = 0.0$ for a thermoelastic MT and lenticular martensite, respectively. As shown by the color bar for e_2, the

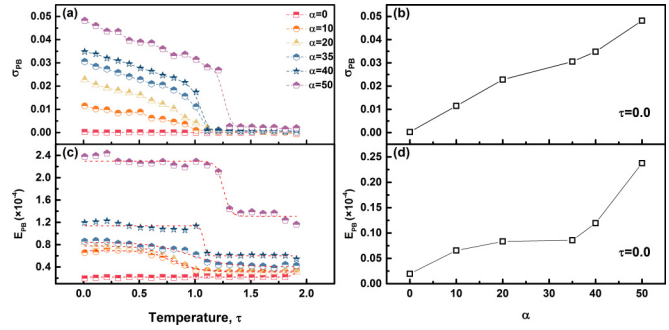

FIG. 8. The temperature dependence of (a) stress (σ_{PB}) and (c) energy (E_{PB}) at the phase boundary between austenite and martensite for different systems with $\alpha = 0$, 10, 20, 35, 40, and 50. (b) and (d) The σ_{PB} and the E_{PB} at temperature $\tau = 0$ as a function of the coupling strength α, respectively.

two variants of martensite are colored in red (positive) and blue (negative) and the austenite with $e_2 = 0$ is in yellow. Similarly, the positive and negative e_1 are in blue and magenta with $e_1 = 0$ white.

The polytwinned microstructure of typical thermoelastic martensite is visible in the e_2 panel and the corresponding distribution of e_1 is quite uniform with e_1 around 0. In contrast, Fig. 7(b) shows lenticular martensite embedded in an austenite matrix in the e_2 panel and a similar e_1 panel. The e_1 for a system with lenticular martensite is no longer trivial. The martensite regions with $e_2 \neq 0$ possess negative e_1 values and the residual austenite regions with e_2 close to 0 have positive e_1 values.

This is easy to see from Eqs. (6) and (4) if one considers the quadratic homogeneous free energy $F = C + A_1 e_1^2 + \alpha e_1 e_2^2$. In equilibrium, $\frac{\partial F}{\partial e_1} = 0$ and the steady state value of e_1 that minimizes the free energy is given by

$$e_1 = -\frac{\alpha e_2^2}{2A_1}. \tag{12}$$

Thus, the magnitude of e_1 is negatively related to the coupling strength α, When the coupling is absent, ($\alpha = 0$), the free energy landscape is symmetric with a minimum at zero, i.e., $e_1 = 0$. Since the coupling coefficient α is positive in the current study, e_1 is negative when the coupling is present. As shown in Fig. 7(b), negative e_1 can be found in the martensite regions. However, the value of e_1 in the residual austenite regions is much larger than zero, indicating that these regions are far from equilibrium. Such nonequilibrium residual austenite is the major difference from the thermoelastic martensite features.

The phase boundary stresses σ_{PB} can be calculated using Eq. (10). As the stress component σ_{yy} behaves similarly to σ_{xx}, we consider σ_{PB} to be σ_{xx} for the mesh points at the phase boundary between austenite and martensite. Equation 8(a) shows σ_{PB} as a function of temperature τ for systems with different coupling strengths.

For $\alpha = 0$, σ_{PB} is trivial before and after the phase transformation. As α increases, σ_{PB} is very small at high temperature and is finite below the transformation temperature. Figure 8(b) shows that σ_{PB} increases monotonically with the coupling strength. The free energy at the boundary, E_{PB}, as a function

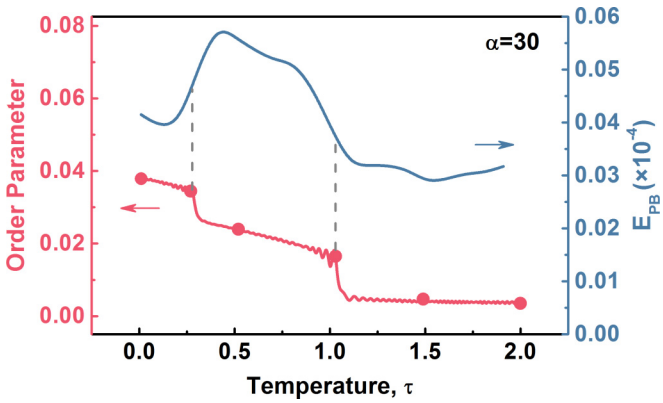

FIG. 9. The order parameter strain e_2 and the energy at the phase boundary E_{PB} of the system with $\alpha = 30$ as a function of temperature τ.

of temperature is plotted in Fig. 11(a) and as a function of α at $\tau = 0$ in Fig. 11(a). Both curves show a similar trend with α.

In the absence of coupling, e_1 is essentially 0 and there is little boundary stress so that self-accomodation is easy to satisfy in thermoelastic MT. With $\alpha \neq 0$, the presence of e_1 enhances the stress at the phase boundary, increasing E_{PB} and arresting the transformation, resulting in the nonthermoelastic martensite microstructure shown in Fig. 7(b).

During the martensitic transformation with nonthermoelastic features, σ_{PB} and E_{PB} prevent free movement of the phase boundary, thus resulting in greater degree of undercooling and superheating to promote the transformation. This causes the thermal hysteresis to increase with increasing α. For systems with large coupling strength, σ_{PB} and E_{PB} are too large to complete the transformation, resulting in residual austenite or martensite. Moreover, the release of σ_{PB} is rather slow and can persist at high temperatures. Thus, during thermal cycling, σ_{PB} accumulates and leads to residual strain at high temperatures.

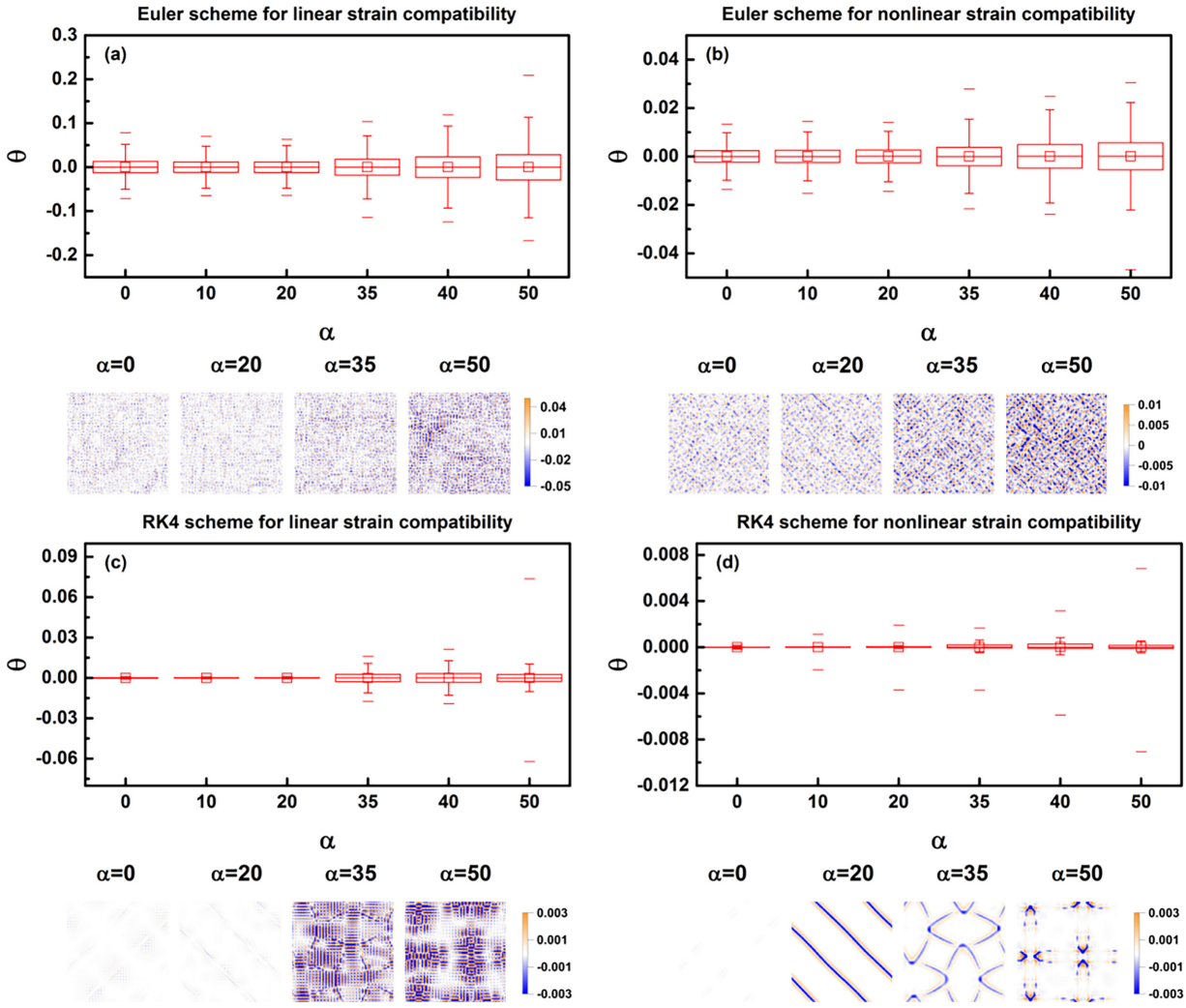

FIG. 10. The average of the elastic compatibility correction, θ, calculated using Eq. (13) (linear strain compatibility) and Eq. (14) (nonlinear strain compatibility) for systems with coupling strengths $\alpha = 0$, 10, 20, 35, 40, and 50 at $\tau = 0.0$. θ is calculated using Euler and fourth-order Runge-Kutta schemes. The distribution of θ is shown in the box chart. The midline in the box represents the median; the little box inside the outer box is the average θ. The whiskers extend from the box to the minimum and maximum values. The dashes away from the whiskers are the limits of the outliers. The average value $\langle\theta\rangle$ over the whole system is essentially zero. The panels at the bottom are the spatial distributions of θ for typical simulations.

As shown in Fig. 4, a two-step phase transformaton occurs with disppearing nonthermoelastic in the system with coupling strength $\alpha = 30$. The order parameter e_2 and the $E_{\rm PB}$ of the system as a function of temperature τ for $\alpha = 30$ are shown in Fig. 9. The value of e_2 increases with decreasing temperature, and two jumps in e_2 were observed. The two anomalies correspond to the transformation from austenite to nonthermoelastic martensite and that from the nonthermoelastic martensite to ideal thermoelastic martensite. The $E_{\rm PB}$ increases for the former transformation, which inhibits the movement of the phase boundary, whereas $E_{\rm PB}$ decreases for the latter transformation as the energy generated during cooling overcomes the effects of e_1. The two-step martensitic transformation behavior has been observed in FePdCo and FePdMn alloys that possess face-centered-cubic to face-centered-tetragonal (fcc-fct) thermoelastic MT and face-centered-tetragonal to body-centered-tetragonal (fct-bct) nonthermoelastic MT at different temperatures [40,41].

B. Validity of strain compatibility due to e_1 and e_2 coupling

The OP strain e_2 and the non-OP strain (e_1 and e_3) are not independent because they are the derivatives of the same underlying displacement field. They satisfy compatibility constraints to ensure lattice integrity. Formally, for small strains, the *linear* constraint is expressed through the Saint-Venant equation in two dimensions,

$$\theta = \nabla^2 e_1 - \left(\frac{\partial^2}{\partial x^2} - \frac{\partial^2}{\partial y^2}\right) e_2 - \sqrt{8}\frac{\partial^2}{\partial x\,\partial y} e_3. \tag{13}$$

If $\theta = 0$, then elastic compatibility is satisfied, whereas $\theta \neq 0$ indicates that there is a source term due to nonlinear effects as a result of the strains not being small and also numerical instability in solving the displacement equations. In real systems dislocations or cracks would violate integrability [42]. We have not incorporated a dislocation field in our model.

The nonlinear strain compatibility equation in 2D, up to second order in strain components, is given by

$$\begin{aligned}\theta = {} & \frac{\partial^2 \epsilon_{xx}}{\partial y^2} + \frac{\partial^2 \epsilon_{yy}}{\partial x^2} - 2\frac{\partial^2 \epsilon_{xy}}{\partial x \partial y} \\ & + \left(-\frac{\partial \epsilon_{xx}}{\partial x}\frac{\partial \epsilon_{yy}}{\partial x} - \frac{\partial \epsilon_{xx}}{\partial y}\frac{\partial \epsilon_{xx}}{\partial y}\right. \\ & + 2\frac{\partial \epsilon_{xx}}{\partial x}\frac{\partial \epsilon_{xy}}{\partial y} - \frac{\partial \epsilon_{yy}}{\partial x}\frac{\partial \epsilon_{yy}}{\partial x} \\ & \left. - \frac{\partial \epsilon_{yy}}{\partial y}\frac{\partial \epsilon_{xx}}{\partial y} + 2\frac{\partial \epsilon_{xy}}{\partial x}\frac{\partial \epsilon_{yy}}{\partial y}\right).\end{aligned} \tag{14}$$

The corresponding expression in terms of e_1, e_2, and e_3 is given in [43]. In order to check the validity of the linear and nonlinear compatibility relations above, we calculated $\langle\theta\rangle$ for $\alpha = 0$, 10, 20, 35, 40, and 50 at $\tau = 0.0$ using both the Euler and fourth-order Runge-Kutta schemes. As Fig. 10 shows, in general the average value $\langle\theta\rangle$ over the whole system is essentially zero; however, locally there are deviations from compatibility which increase with coupling strength α. In general, the correction to linear compatibility is an order of magnitude larger than for the nonlinear case using Euler. With RK4, these corrections are an order of magnitude even smaller than Euler. The Euler results for the nonlinear compatibility are comparable to the RK4 results for linear compatibility. Thus, both the precision of the numerical scheme and the nonlinear terms in strain compatibility need to be taken into account when checking compatibility. The four panels at the bottom show the spatial distribution of θ for different coupling strengths, $\alpha = 0$, 20, 35, and 50 as calculated by Euler and RK4 for linear and nonlinear compatibility. The RK4 results illustrate that deviations from compatibility are greatest at domain walls where there are large changes in strains.

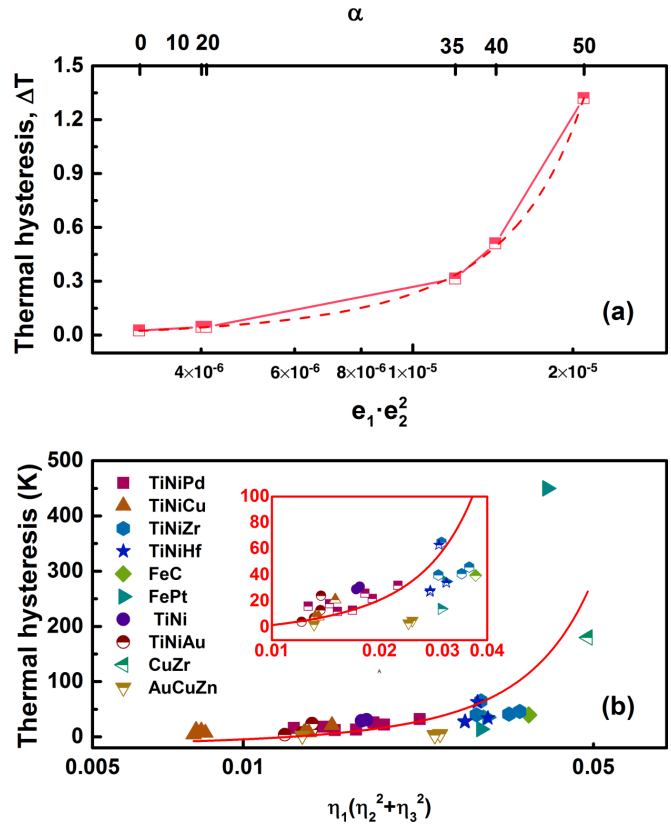

FIG. 11. (a) The thermal hysteresis ΔT as a function of $e_1 e_2^2$ as well as α from our simulation results. With α increasing, $e_1 e_2^2$ increases and so does the thermal hysteresis ΔT. The dotted line is the fit to the data based on exponential growth, $\Delta T = -0.12 + 0.1e^{128524(e_1 e_2^2)}$. (b) The experimental results on the thermal hysteresis as a function of $\eta_1(\eta_2^2 + \eta_3^2)$ follow the same the exponential form, $\Delta T = -18 + 10e^{68[\eta_1(\eta_2^2+\eta_3^2)]}$.

When the coupling coefficient α is 0, 10, and 20, the spatial distribution of θ is fairly uniform. Therefore, in these simulations, the elastic compatibility condition for strains is satisfied. However, with increasing α, the spatial distribution is rather uneven as the larger values of e_1 during the martensitic transformation make it difficult to always locally satisfy compatibility over the timescales of the simulations [44,45]. Therefore, in systems with nonthermoelastic features, continuity inside the microstructure is instantaneously not satisfied. This would in a real martensite lead to nucleation of dislocations [46,47].

C. A materials descriptor associated with the martensitic transformation

In our model, the thermoelastic martensite and non-thermoelastic martensite features are distinguished by the coupling term $\alpha e_1 e_2^2$. A larger coupling strength leads to features of nonthermoelastic martensite. Therefore, we can consider the coupling term $e_1 e_2^2$ as a materials descriptor to describe and predict thermal hysteresis.

Figure 11(a) shows how the thermal hysteresis changes with the coupling $e_1 e_2^2$ and with the coupling strength α based on our simulation results. We find that $e_1 e_2^2$ of martensite increases with increasing α, and the thermal hysteresis also increases consistently. The same exponential form can fit the thermal hysteresis as a function of $e_1 e_2^2$, which gives $\Delta T = -0.12 + 0.1e^{128524(e_1 e_2^2)}$.

For real materials undergoing a simple cubic to tetragonal, tetragonal to orthorhombic, or face-centered-cubic to face-centered-tetragonal transformation, the lattice parameters a_0 for austenite and a, b, c for martensite can be used used to calculate the symmetry adapted strains $\eta_1 = (\varepsilon_{11} + \varepsilon_{22} + \varepsilon_{33})/\sqrt{3}$, $\eta_2 = (\varepsilon_{11} - \varepsilon_{22})/\sqrt{2}$, and $\eta_3 = (\varepsilon_{11} + \varepsilon_{22} - 2\varepsilon_{33})/\sqrt{6}$, where the strain components are $\varepsilon_{11} = 1 + \frac{a-a_0}{a_0}$, $\varepsilon_{22} = 1 + \frac{b-\sqrt{2}a_0}{\sqrt{2}a_0}$, and $\varepsilon_{33} = 1 + \frac{c-\sqrt{2}a_0}{\sqrt{2}a_0}$ [48]. η_2 and η_3 are both deviatoric strains, and η_1 is the volume strain. We then form the requisite symmetry allowed combination $\eta_1(\eta_2^2 + \eta_3^2)$ to explore whether the relationship is satisfied experimentally.

Figure 11(b) shows the experimental thermal hysteresis as a function of $\eta_1(\eta_2^2 + \eta_3^2)$ for different martensitic alloys [48–60]. The experimental results on the thermal hysteresis as a function of $\eta_1(\eta_2^2 + \eta_3^2)$ follow the same the exponential form, $\Delta T = -18 + 10e^{68[\eta_1(\eta_2^2+\eta_3^2)]}$. Thus, a very similar trend can be seen for both our simulation results and the experimental results.

V. SUMMARY

In summary, we have introduced a coupling between the non-order parameter volumetric strain and the order parameter deviatoric shear strain into the free energy of a Landau model to investigate non-thermoelastic features in an ideal thermoelastic martensitie. The model reproduces features of both types of transformations, including (1) the change of thermal hysteresis, transformation temperature and residual strain, (2) the microstructure evolution and (3) the thermal cycling behavior. The coupling accentuates e_1 during the transformation, which greatly enhances the stress and energy at the phase boundary and effectively gives rise to a source term in strain compatibility which would nucleate dislocations. Our simulations show the emergence of non-thermoelastic features in our thermoelastic martensitic model, and the coupling can serve as a materials descriptor for thermal hysteresis. Although most known martensitic alloys exhibit non-thermoelastic features only as a result of nucleating dislocations, we speculate that alloys with high elastic limits may show similar behavior. For example, high entropy shape memory alloys with high strength and large hysteresis, such as $Ti_{20}Hf_{15}Zr_{15}Cu_{25}Ni_{25}$ [61], $(TiZrHf)_{50}Ni_{25}Co_{10}Cu_{15}$ [62,63] are potential candidates for this type of behavior.

ACKNOWLEDGMENTS

The authors gratefully acknowledge the support of National Natural Science Foundation of China (Grants No. 51931004, No. 52173228, and No. 52271190), National Key Research and Development Program of China (2021YFB3802102), and the 111 project 2.0 (BP2018008).

[1] K. Otsuka and X. Ren, Physical metallurgy of TiNi-based shape memory alloys, Prog. Mater. Sci. **50**, 511 (2005).
[2] E. Salje, Phase transitions in ferroelastic and co-elastic crystals, Ferroelectrics **104**, 111 (1990).
[3] M. X. Zhang and P. M. Kelly, Crystallographic features of phase transformations in solids, Prog. Mater. Sci. **54**, 1101 (2009).
[4] P. M. Kelly and L. R. F. Rose, The martensitic transformation in ceramics—its role in transformation toughening, Prog. Mater. Sci. **47**, 463 (2002).
[5] S. Deville and J. Chevalier, Martensitic relief observation by atomic force microscopy in yttria-stabilized zirconia, J. Am. Ceram. Soc. **86**, 2225 (2003).
[6] T. Teramoto, K. Nagahira, and K. Tanaka, Geometry and energy barrier of martensite in the initial stage martensitic transformation in B19'TiNi shape memory alloy, Acta Mater. **201**, 94 (2020).
[7] D. Dunne, Shape memory in ferrous alloys, in *Phase Transformations in Steels* (Woodhead, Oxford, 2012), p. 83.
[8] L. Jian, C. C. Chou, and C. M. Wayman, Martensitic transformation and the shape memory effect in an $Fe_{33}Ni_{12}Co_5Ti$ alloy, Mater. Chem. Phys. **34**, 14 (1993).
[9] R. Santamarta, R. Arróyave, J. Pons, A. Evirgen, I. Karaman, H. Karaca, and R. Noebe, TEM study of structural and microstructural characteristics of a precipitate phase in Ni-rich NiTiHf and NiTiZr shape memory alloys, Acta Mater. **61**, 6191 (2013).
[10] T. Omori, M. Nagasako, M. Okano, K. Endo, and R. Kainuma, Microstructure and martensitic transformation in the FeMnAlNi shape memory alloy with B2-type coherent fine particles, Appl. Phys. Lett. **101**, 231907 (2012).
[11] P. Hua, M. Xia, Y. Onuki, and Q. Sun, Nanocomposite NiTi shape memory alloy with high strength and fatigue resistance, Nat. Nanotechnol. **16**, 409 (2021).
[12] K. C. Atli, B. E. Franco, I. Karaman, D. Gaydosh, and R. D. Noebe, Influence of crystallographic compatibility on residual strain of TiNi based shape memory alloys during thermo-mechanical cycling, Mater. Sci. Eng. A **574**, 9 (2013).
[13] S. Belyaev, N. Resnina, and A. Sibirev, Peculiarities of residual strain accumulation during thermal cycling of TiNi alloy, J. Alloys Compd. **542**, 37 (2012).
[14] M. Umemoto and C. Wayman, Crystallography and morphology studies of FePt martensites: Lenticular to thin plate

transition and thin plate morphologies, Acta Metall. **26**, 1529 (1978).
[15] A. Roitburd, Martensitic transformation as a typical phase transformation in solids, in *Solid State Physics* (Elsevier, Amsterdam, 1978), Vol. 33, pp. 317–390.
[16] V. A. Lobodyuk, Reversibility of the martensitic transformations and shape-memory effects, Usp. Fiz. Met. **17**, 89 (2016).
[17] M. Umemoto and W. CM, Irreversible lattice defects formed by martensitic transformation cycles in a nearly thermoelastic FePt alloy, Trans. Jpn. Inst. Met. **19**, 281 (1978).
[18] Y. Tanaka, Y. Himuro, R. Kainuma, Y. Sutou, T. Omori, and K. Ishida, Ferrous polycrystalline shape-memory alloy showing huge superelasticity, Science **327**, 1488 (2010).
[19] M. Vojtko and S. Longauer, Study of decomposition of thermoelastic and non-thermoelastic martensite in CuZnAl alloys, in *European Symposium on Martensitic Transformations* (EDP Sciences, Les Ulis. France, 2009), p. 02035.
[20] M. Bouville and R. Ahluwalia, Effect of lattice-mismatch-induced strains on coupled diffusive and displacive phase transformations, Phys. Rev. B **75**, 054110 (2007).
[21] E. Pereloma and D. V. Edmonds, *Phase Transformations in Steels: Diffusionless Transformations, High Strength Steels, Modelling and Advanced Analytical Techniques* (Elsevier, Amsterdam, 2012).
[22] T. Tadaki, Phenomenological consideration on the change from the non-thermoelastic to the thermoelastic type of martensitic transformations in Fe_3Pt alloy, Trans. Jpn. Inst. Met. **18**, 864 (1977).
[23] M. Umemoto and C. Wayman, The effect of austenite ordering on the transformation temperature, transformation hysteresis, and thermoelastic behavior in FePt alloys, Metall. Trans. A **9**, 891 (1978).
[24] M. Tang, J. Zhang, and T. Hsu, One-dimensional model of martensitic transformations, Acta Mater. **50**, 467 (2002).
[25] Y. Yang, D. Xue, R. Yuan, Y. Zhou, T. Lookman, X. Ding, X. Ren, and J. Sun, Doping effects of point defects in shape memory alloys, Acta Mater. **176**, 177 (2019).
[26] P. Lloveras, T. Castán, M. Porta, A. Planes, and A. Saxena, Influence of Elastic Anisotropy on Structural Nanoscale Textures, Phys. Rev. Lett. **100**, 165707 (2008).
[27] S. R. Shenoy, T. Lookman, A. Saxena, and A. R. Bishop, Martensitic textures: Multiscale consequences of elastic compatibility, Phys. Rev. B **60**, R12537(R) (1999).
[28] R. Ahluwalia, T. Lookman, and A. Saxena, Dynamic strain loading of cubic to tetragonal martensites, Acta Mater. **54**, 2109 (2006).
[29] D. Xue, Y. Zhou, X. Ding, T. Lookman, J. Sun, and X. Ren, Aging and deaging effects in shape memory alloys, Phys. Rev. B. **86**, 184109 (2012).
[30] S. Kartha, J. A. Krumhansl, J. P. Sethna, and L. K. Wickham, Disorder-driven pretransitional tweed pattern in martensitic transformations, Phys. Rev. B **52**, 803 (1995).
[31] N. Nakada, Direct observation of martensitic reversion from lenticular martensite to austenite in FeNi alloy, Mater. Lett. **187**, 166 (2017).
[32] L. Del-Río, M. L. Nó, A. Sota, I. Perez-Casero, J. F. Gómez-Cortés, M. Pérez-Cerrato, A. Veiga, I. Ruiz-Larrea, S. Ausejo, N. Burgos, and J. M. San Juan, Internal friction associated with ε martensite in shape memory steels produced by casting route and through additive manufacturing: Influence of thermal cycling on the martensitic transformation, J. Alloys Compd. **919**, 165806 (2022).
[33] T. Maki, S. Furutan, and I. Tamura, Shape memory effect related to thin plate martensite with large thermal hysteresis in ausaged Fe-Ni-Co-Ti alloy, ISIJ Int. **29**, 438 (1989).
[34] T. Omori, S. Abe, Y. Tanaka, D. Y. Lee, K. Ishida, and R. Kainuma, Thermoelastic martensitic transformation and superelasticity in Fe–Ni–Co–Al–Nb–B polycrystalline alloy, Scr. Mater. **69**, 812 (2013).
[35] S. Matsumoto, A. Sato, and T. Mori, Formation of h.c.p. and f.c.c. twins in an FeMnCrSiNi alloy, Acta Metall. Mater. **42**, 1207 (1994).
[36] K. Bhattacharya, S. Conti, G. Zanzotto, and J. Zimmer, Crystal symmetry and the reversibility of martensitic transformations, Nature (London) **428**, 55 (2004).
[37] J. M. Logan, Laboratory and case studies of thermal cycling and stored strain on the stability of selected marbles, Environ. Geol. **46**, 456 (2004).
[38] G. Robert Humfeld, Jr., and D. A. Dillard, Residual stress development in adhesive joints subjected to thermal cycling, J. Adhesion **65**, 277 (1998).
[39] C. B. Churchill, Sensing of retained martensite during thermal cycling of shape memory alloy wires via electrical resistance, Proc. SPIE **8689**, 868912 (2013).
[40] F. G. Bonifacich, O. A. Lambri, D. Gargicevich, G. I. Zelada, J. I. Pérez-Landazábal, V. Recarte, and V. Sánchez-Alarcos, Influence of defects on the irreversible phase transition in the Fe-Pd doped with Co and Mn, Matéria (Rio J.) **23** (2018).
[41] R. Oshima and M. Sugiyama, Martensite transformations in Fe–Pd alloys, J. Phys. Colloq. **43**, C4-383 (1982).
[42] T. Lookman, S. R. Shenoy, K. O. Rasmussen, A. Saxena, and A. R. Bishop, Ferroelastic dynamics and strain compatibility, Phys. Rev. B **67**, 024114 (2003).
[43] M. Porta and T. Lookman, Heterogeneity and phase transformation in materials: Energy minimization, iterative methods and geometric nonlinearity, Acta Mater. **61**, 5311 (2013).
[44] J. R. Barber, *Elasticity* (Springer, New York, 2002).
[45] C. Amrouche, P. G. Ciarlet, L. Gratie, and S. Kesavan, On Saint Venant's compatibility conditions and Poincaré's lemma, C. R. Math. **342**, 887 (2006).
[46] E. J. Suoninen, Investigation of the martensitic transformation in metastable beta brass, Ph.D. thesis, Massachusetts Institute of Technology, 1954.
[47] G. Olson and M. Cohen, A perspective on martensitic nucleation, Annu. Rev. Mater. Sci. **11**, 1 (1981).
[48] T. H. Nam, T. Saburi, Y. Nakata, and K. Shimizu, Shape memory characteristics and lattice deformation in Ti–Ni–Cu alloys, Mater. Trans. JIM **31**, 1050 (1990).
[49] R. Delville, S. Kasinathan, Z. Zhang, J. V. Humbeeck, R. D. James, and D. Schryvers, Transmission electron microscopy study of phase compatibility in low hysteresis shape memory alloys, Philos. Mag. **90**, 177 (2010).
[50] A. Evirgen, I. Karaman, R. Santamarta, J. Pons, C. Hayrettin, and R. Noebe, Relationship between crystallographic compatibility and thermal hysteresis in Ni-rich NiTiHf and NiTiZr high temperature shape memory alloys, Acta Mater. **121**, 374 (2016).
[51] J. Mazur, Lattice parameters of martensite and of austenite, Nature (London) **166**, 828 (1950).

[52] V. Lobodyuk, Y. Meshkov, E. V. Pereloma *et al.*, On tetragonality of the martensite crystal lattice in steels, Metall. Mater. Trans. A **50**, 97 (2019).

[53] X. Hao and H. Ohtsuka, Effects of a high magnetic field on transformation temperatures in Fe-based alloys, ISIJ Int. **46**, 1271 (2006).

[54] T. Tadaki and K. Shimizu, High tetragonality of the thermoelastic Fe_3Pt martensite and small volume change during the transformation, Scr. Metall. **9**, 771 (1975).

[55] H. Shi, R. Delville, V. Srivastava, R. James, and D. Schryvers, Microstructural dependence on middle eigenvalue in TiNiAu, J. Alloys Compd. **582**, 703 (2014).

[56] Y. Song, X. Chen, V. Dabade, T. W. Shield, and R. D. James, Enhanced reversibility and unusual microstructure of a phase-transforming material, Nature (London) **502**, 85 (2013).

[57] X. Fu, G. Wang, Y. Wu, W. Song, C. H. Shek, Y. Zhang, J. Shen, and R. O. Ritchie, Compressive ductility and fracture resistance in CuZr-based shape-memory metallic-glass composites, Int. J. Plast. **128**, 102687 (2020).

[58] C. Biffi, M. Coduri, H. Yoshida, Y. Soejima, M. Nishida, and A. Tuissi, The effect of thermal cycling on the martensitic transformation in equiatomic CuZr shape memory alloy, J. Alloys Compd. **653**, 591 (2015).

[59] J. K. Stalick and R. M. Waterstrat, Crystal structures and phase equilibria in the hafnium-palladium system, J. Phase Equilibria Diffus. **37**, 416 (2016).

[60] I. Kaya, E. Acar, and H. Karaca, Phase transformation and mechanical properties of HfPd ultra-high temperature shape memory alloys, Appl. Phys. A **125**, 442 (2019).

[61] S. Li, D. Cong, Z. Chen, S. Li, C. Song, Y. Cao, Z. Nie, and Y. Wang, A high-entropy high-temperature shape memory alloy with large and complete superelastic recovery, Mater. Res. Lett. **9**, 263 (2021).

[62] C. H. Chen and Y. J. Chen, Shape memory characteristics of $(TiZrHf)_{50}Ni_{25}Co_{10}Cu_{15}$ high entropy shape memory alloy, Scr. Mater. **162**, 185 (2019).

[63] J. Yaacoub, W. Abuzaid, F. Brenne, and H. Sehitoglu, Superelasticity of $(TiZrHf)_{50}Ni_{25}Co_{10}Cu_{15}$ high entropy shape memory alloy, Scr. Mater. **186**, 43 (2020).